

Quasiparticle band alignment and stacking-independent exciton in MA_2Z_4 ($\text{M} = \text{Mo}, \text{W}, \text{Ti}$; $\text{A} = \text{Si}, \text{Ge}$; $\text{Z} = \text{N}, \text{P}, \text{As}$)

Hongxia Zhong,^{1*} Guangyong Zhang,¹ Cheng Lu,¹ Shiyuan Gao^{2*}

¹*School of Mathematics and Physics, China University of Geosciences, Wuhan 430074, China and*

²*Institute for Quantum Matter and Department of Physics and Astronomy, Johns Hopkins University, Baltimore, Maryland 21218, USA**

Motivated by the recently synthesized two-dimensional semiconducting MoSi_2N_4 , we systematically investigate the quasiparticle band alignment and exciton in monolayer MA_2Z_4 ($\text{M} = \text{Mo}, \text{W}, \text{Ti}$; $\text{A} = \text{Si}, \text{Ge}$; $\text{Z} = \text{N}, \text{P}, \text{As}$) using ab initio GW and Bethe-Salpeter equation calculations. Compared with the results from density functional theory (DFT), our GW calculations reveal substantially larger band gaps and different absolute quasiparticle energies, but predict the same types of band alignments. Using $\text{MoSi}_2\text{N}_4/\text{WSi}_2\text{N}_4$ heterostructure as a model, we find that the quasiparticle band energies are insensitive to environmental screening, with band edge energies changing about 0.15 eV, leading to a $\sim 4\%$ reduction in the quasiparticle band gap compared to free-standing monolayers. Finally, inspired by recent interests in moiré excitons, we study quasiparticle and exciton properties of $\text{MoSi}_2\text{N}_4/\text{WSi}_2\text{N}_4$ bilayers with different stacking configurations. The optical dipole oscillator strength and energy of intralayer excitons are almost independent of the stacking configuration, while the interlayer exciton is dark due to negligible electron-hole overlap. The quasiparticle band alignment and stacking-independent exciton obtained in this work are important for designing heterojunction and high-efficiency optoelectronic devices based on MA_2Z_4 .

I. INTRODUCTION

Owing to the depressed screening and strong electron-electron interactions, many-electron effects are more pronounced in two-dimensional (2D) materials compared with their bulk phases[1–4]. The enhanced many-electron effects are expected to increase the quasiparticle band gap and cause electron-hole pairs to form strongly bound excitons[5, 6]. Indeed, for most 2D semiconductors, the quasiparticle band gaps are larger than the single particle band gaps by 0.5-2 eV, and the exciton binding energies are at least an order magnitude larger than those of bulk structures[5–7]. Besides the precise band gap, the relative band edge energies between different semiconductors and corresponding band alignments are desirable for understanding fundamental physics and designing heterojunction devices[8, 9].

During the process of 2D material growth, it needs a substrate, and the environmental screening from the substrate will significantly renormalize the quasiparticle band gap and exciton binding energy of the atomically thin system[1, 10, 11]. For example, when black phosphorus is encapsulated between sapphire and h -BN, the substrate screening of sapphire reduces the binding energy of monolayer black phosphorus by as much as 70% and completely eliminates the presence of bound excitons in four-layer black phosphorus[10, 12–14]. By stacking two monolayers together, van der Waals heterostructures are formed, inheriting and extending the physical properties of the original monolayers[15–17]. Each layer of the heterostructure has different orientations, and the relative orientation between two layers of a 2D crystal introduces

a longer-period variation of local atomic arrangement, which is known as the moiré pattern[18, 19]. It has been demonstrated that the transition-metal dichalcogenide (TMDC) heterobilayer moiré pattern can modulate the electronic band structure and induce multiple interlayer exciton resonances in experiments[16, 18, 20]. Therefore, the effect of environmental screening and moiré pattern on quasiparticle band alignment and excitons are of fundamental interest in 2D semiconductors.

Here, we focus on the quasiparticle band alignment and exciton properties of the recently synthesized semiconducting MoSi_2N_4 and its family[21, 22], which is a member of another new family of 2D molybdenum nitrides without bulk phases. Monolayer MoSi_2N_4 shows an optical gap of ~ 1.94 eV, and high intrinsic electron carrier mobilities ($1200 \text{ cm}^2/(\text{v}\cdot\text{s})$)[21]. The excellent mechanical properties and ambient stability of monolayer MoSi_2N_4 have inspired much follow-up works, and a number of interesting properties such as spin-valley coupling[23–25], high thermal conductivity[26], and piezoelectricity[27] have been predicted. However, the quasiparticle band alignment of monolayer MA_2Z_4 has yet to be studied, and the effect of environmental screening and moiré pattern on quasiparticle band alignment and excitons is unknown.

In this work, we will fill in these blanks theoretically by first-principles GW-Bethe Salpeter equation (BSE) approach. Based on the electronic structure details, we discuss the absolute quasiparticle band alignment of monolayer MA_2Z_4 ($\text{M} = \text{Mo}, \text{W}, \text{Ti}$; $\text{A} = \text{Si}, \text{Ge}$; $\text{Z} = \text{N}, \text{P}, \text{As}$) and compare it with the result from density functional theory (DFT). It is found that the band-gap-center model is valid for the studied monolayer MA_2Z_4 , leading to the same types of band alignments predicted by both GW and DFT calculations. We then study the environmental screening on the band alignment using the model

* zhonghongxia@cug.edu.cn; sgao45@jh.edu

MoSi₂N₄/WSi₂N₄ heterostructure, and find the quasiparticle band gap renormalization is very small, suggesting the weak environmental screening effect on the quasiparticle band alignments of MA₂Z₄. Finally, we focus on the excitons in MoSi₂N₄/WSi₂N₄ heterostructure with three local identified stackings to discuss the effect of moiré pattern. The optical dipole oscillator strength and energy of intralayer excitons are almost independent of the stacking configuration, while the interlayer exciton is dark owing to negligible electron-hole overlap.

The remainder of this paper is organized as follows: In Sec. II, we introduce the atomic structures of monolayer MA₂Z₄, and our computational approaches. In Sec. III, the quasiparticle band gap and electronic structure details are presented. In Sec. IV, the quasiparticle band alignment is given. In Sec. V, we discuss the environmental screening effect on the quasiparticle band alignment of monolayer MA₂Z₄. In Sec. VI, we focus on the low-energy excitons in MoSi₂N₄/WSi₂N₄ heterostructure with different stackings. Finally, the conclusion is summarized in Sec. VII.

II. ATOMIC STRUCTURE AND CALCULATION METHOD

Compared with hexagonal TMDC, monolayer MA₂Z₄ also belongs to the hexagonal lattice but with lower symmetry (space group P $\bar{6}$ m2 (No. 187)), as shown in Fig. 1. Along the *z* direction, it has a septuple atomic layers of Z-A-Z-M-Z-A-Z, which can be viewed as a MZ₂ layer passivated by two A-Z bilayers, leading to the excellent ambient stability of MA₂Z₄ monolayers[21]. We fully relax monolayer MA₂Z₄ (M = Mo, W, Ti; A = Si, Ge; Z = N, P, As) according to the force and stress calculated by density functional theory (DFT) with the Perdew, Burke, and Ernzerhof (PBE) functional[28], using the QUANTUM ESPRESSO package[29]. The van der Waals corrections (vdW-DF) are utilized to include the interlayer interaction in the constructed heterostructures[30]. The ground state wave functions and eigenvalues are obtained from the DFT/PBE with norm-conserving pseudopotentials which include the semi-core states of transition metal M[31]. The plane-wave basis is set with a cutoff energy of 80 Ry with a 16 × 16 × 1 *k*-point grid. A vacuum space between neighboring layers is set to be more than 25 Å to avoid interactions between layers. Based on these parameters, the relaxed lattice constant for monolayer MoSi₂N₄ (2.910 Å) is in good agreement with previous calculations[21, 32]. The optimized lattice constants of MA₂Z₄ are summarized in Table I. One can see that the lattice constant increases as the radius of A or Z atoms increases. For example, the lattice constant increases from 2.910 Å in MoSi₂N₄ to 3.469 Å in MoSi₂P₄ to 3.617 Å in MoSi₂As₄, in agreement with increasing trend of the atomic radius of Z atoms. And the lattice constant of MoGe₂N₄ (3.035 Å) is slightly larger than that (2.910 Å) of MoSi₂N₄, owing to the slightly larger atomic ra-

dius of Ge than Si atom. On the contrary, the lattice constant is nearly not affected by the M atom, which is always around 2.920 Å for all MSi₂N₄ (M = Mo, W, Ti) monolayer. Therefore, primitive MSi₂N₄ monolayer can be adjusted to other MSi₂N₄ unit cell, forming heterostructures with negligible lattice mismatch.

The excited-state properties of the heterostructure are calculated by the GW approximation within the general plasmon pole model[33], which is reliable in obtaining the excitonic properties of 2D materials. The unoccupied conduction band number involved in calculating the dielectric function, self-energy, and absolute band edge is set to be 2000 after converge test. In solving the BSE, we use a finer *k*-point grid of 48 × 48 × 1 for converged excitonic states[34]. All the GW-BSE calculations are performed with the BerkeleyGW code[35] including the slab Coulomb truncation scheme to mimic interactions between structures[36, 37]. For optical absorption spectra, only the incident light polarized parallel with the plane is considered due to the depolarization effect[38, 39].

III. ELECTRONIC STRUCTURES

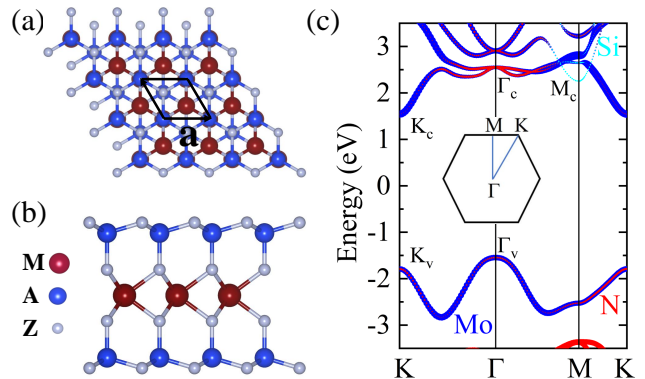


FIG. 1. Top (a) and side (b) views of atomic structure of monolayer MA₂Z₄. The primitive cell and lattice vector **a** are labeled in (a). Quasiparticle band structure (c) of monolayer MoSi₂N₄. The band gap center is set to be zero. Two highest valence band states K_v and Γ_v, and three lowest conduction band states K_c, Γ_c, and M_c are labeled. Here, we define the energy difference Γ_v - K_v as Δ_v, and the energy difference Γ_c - K_c (M_c - K_c) as Δ_{c1} (Δ_{c2}).

We plot the quasiparticle band structure of monolayer MoSi₂N₄ in Fig. 1c as an example to discuss the general electronic features of studied MA₂Z₄ (M = Mo, W, Ti; A = Si, Ge; Z = N, P, As). It is shown that monolayer MoSi₂N₄ is an indirect bandgap semiconductor, with valence band maximum (VBM) at the Γ point and conduction band minimum (CBM) at the K point. There is another local maximum of the valence band at the K point, whose energy is very close to the VBM at the Γ point. Actually, this local maximum at the K point can increase to become the VBM in monolayer MoSi₂P₄

and MoSi_2As_4 , and thus, the overall band structure turns out to possess a direct band gap[21], which displays much stronger photoluminescence accordingly. In order to analyze this subtle but important change in band structure, we define quantitatively the energy difference between the two highest valence band states $\Gamma_v - K_v$ as Δ_v (see Fig. 1c), and summarize its values in Table I.

We first discuss the energy difference at the DFT level. The positive value of Δ_v means the indirect band gap, and the negative value in monolayer MoSi_2P_4 and MoSi_2As_4 means the direct band gap. For most MA_2Z_4 , the Δ_v value is positive and larger than 200 meV, which can be comparable to those in monolayer TMDC. Meanwhile, we have marked the energy difference Δ_{c1} (Δ_{c2}) between the lowest conduction band states $\Gamma_c - K_c$ ($M_c - K_c$), and listed their values in Table I. Compared with the Δ_v values, the values of Δ_{c1} and Δ_{c2} are much larger, ranging from 0.681 to 1.919 eV, except for the Δ_{c2} in monolayer WSi_2N_4 . The large energy difference is attributed to the strong hybridization of lowest conduction band. The K_c state is dominated by M atoms, and Γ_c state is mainly contributed by Z atoms, while M_c state only contains A atoms (see Fig. 1c). It is the hybridized lowest conduction band that results in the dispersive CBM[21], which is very different from the balanced carrier mobility in TMDC.

Owing to the depressed screening and stronger electron-electron (e-e) interactions[1–4], significant self-energy enhancements are expected to be observed in monolayer MA_2Z_4 . We thus apply the single-shot G_0W_0 approach to calculate the quasiparticle energy of those six monolayer MA_2Z_4 (M = Mo, W, Ti; A = Si, Ge; Z = N, P, As), and summarize the results in Table I. First, our calculated G_0W_0 band gap (3.090 eV) of monolayer MoSi_2N_4 is in good agreement with the value (3.190 eV) in previous studies[40]. Second, the GW correction significantly enlarges the bandgap for all studied MA_2Z_4 . At the G_0W_0 level, the quasiparticle band gap of monolayer MA_2Z_4 is increased by 0.5-1.3 eV. Finally, the G_0W_0 band gap is significantly larger than HSE value (2.297 eV), while the measured A excitonic transition is around 2.3 eV[21]. Compared with the invalid HSE calculation, the GW band gap may explain (see Section VI) the experimental photoluminescence spectra, verifying the important many body effects in monolayer MA_2Z_4 .

Beside the band gap, we also discuss the effect of self-energy enhancements on the energy difference in Table I. Overall, the quasiparticle correction does not modify the sign of Δ_v , due to the similar quasiparticle correction of M d_{z^2} states for the whole highest valence band in monolayer MA_2Z_4 . In details, for direct semiconductors ($\Delta_v < 0$), the Δ_v value is enhanced by the quasiparticle correction. The quasiparticle energy difference Δ_v of monolayer MoSi_2P_4 (MoSi_2As_4) increases from -0.251 (-0.199) eV at DFT level to -0.605 (-0.522) eV by GW calculation. By contrast, the Δ_v value for indirect semiconductors ($\Delta_v > 0$) is not significantly modified by the quasiparticle corrections. While for the lowest conduc-

tion band, the Δ_{c1} and Δ_{c2} are reduced by the quasiparticle corrections. These different self-energy corrections are caused by the nature of the involved electronic states K_c , Γ_c , and M_c . Generally, the localized electronic states enhance the overlap between wave functions and screened Coulomb interactions, resulting in a large self-energy[6]. Therefore, the quasiparticle energy of the K_c state (dominated by M d_{z^2} states) is enhanced more, and the energy level is heightened more, leading to the reduction in Δ_{c1} and Δ_{c2} after quasiparticle correction.

IV. QUASIPARTICLE BAND ALIGNMENT

It is well known that relative band edge energies between different semiconductors and corresponding band offsets are of fundamental interest in solid state physics and are indispensable for the design of heterojunction devices[8, 9]. We thus calculate the absolute band edge energy relative to the vacuum level. The absolute band edge energy at the DFT level is aligned with the vacuum level, which is set to zero. With the inclusion of self-energy corrections to the DFT eigenvalues, we obtain the absolute quasiparticle energy relative to the vacuum level. Because the convergence of the absolute quasiparticle band edge energy is slower than the band gap convergence, the GW calculations on the absolute quasiparticle band edge energy have to be checked carefully on the k grid and empty bands to get reliable results. We increase k -point grid to $16 \times 16 \times 1$ for relaxation and $48 \times 48 \times 1$ for static calculations, and empty bands to 2000, and find that the absolute quasiparticle band edge energy changes slightly (~ 0.1 eV). Therefore, we calculate the quasiparticle band edge energy based on the above converge parameters.

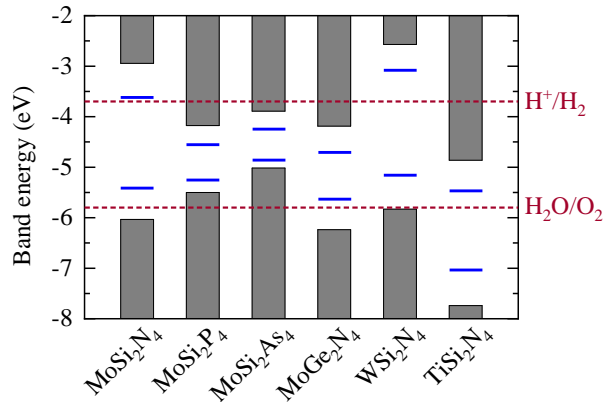


FIG. 2. The absolute band edge energies of calculated monolayer MA_2Z_4 relative to the vacuum level. The grey-shadow regions (blue dashed lines) stand for the fully converged GW (DFT) results. The water reduction (H^+/H_2) and oxidation ($\text{H}_2\text{O}/\text{O}_2$) are marked by the red dashed lines, respectively.

Figure 2 presents the absolute quasiparticle band edge energies of monolayer MA_2Z_4 (M = Mo, W, Ti; A =

TABLE I. Lattice constant a , band gap E_g , energy difference Δ_v , Δ_{c1} , and Δ_{c2} (see Fig. 1c) for monolayer MA_2Z_4 ($M = \text{Mo}, \text{W}, \text{Ti}$; $A = \text{Si}, \text{Ge}$; $Z = \text{N}, \text{P}, \text{As}$).

	a (Å)	E_g^{DFT} (eV)	E_g^{GW} (eV)	Δ_v^{DFT} (eV)	Δ_v^{GW} (eV)	Δ_{c1}^{DFT} (eV)	Δ_{c1}^{GW} (eV)	Δ_{c2}^{DFT} (eV)	Δ_{c2}^{GW} (eV)
MoSi ₂ N ₄	2.910	1.796	3.090	0.309	0.233	1.029	1.074	0.681	0.296
MoSi ₂ P ₄	3.469	0.701	1.324	-0.251	-0.605	1.919	1.418	0.705	0.054
MoSi ₂ As ₄	3.617	0.612	1.126	-0.199	-0.522	1.846	1.244	0.710	0.684
MoGe ₂ N ₄	3.035	0.927	2.052	0.601	0.547	1.001	0.739	1.404	1.672
WSi ₂ N ₄	2.912	2.079	3.018	0.278	0.207	0.813	0.958	0.172	-0.212
TiSi ₂ N ₄	2.932	2.079	3.261	0.336	1.02	0.442	0.505	-0.726	-1.081

Si, Ge; $Z = \text{N}, \text{P}, \text{As}$), in which the DFT results are also listed for reference. First, the values of GW calculated band offsets are larger than those from DFT owing to the large quasiparticle band gap correction. Second, the general trend of the evolution of the band edge energies is similar for both DFT and GW results. For instance, the VBM of monolayer MA_2Z_4 gradually increases as Z varies from N to P to As , or M varies from Mo to W . As a result, the qualitative types of band alignments for these MA_2Z_4 from DFT have not changed. Both DFT and GW calculations predict that the MoSi₂N₄/WSi₂N₄ (MoSi₂N₄/MoSi₂As₄) heterostructure has a type-II (type-I) band alignment. Third, monolayer MoSi₂N₄ and WSi₂N₄ are suitable for water splitting, as a result of lower VBM (higher CBM) than the oxidation energy of -5.8 eV (reduction energy of -3.7 eV)[41]. Finally, both MoSi₂N₄ and WSi₂N₄ are hardly doped n-type owing to their quasiparticle CBMs above the pinning energy of -4.0 eV, but easily doped p-type because of the suitable quasiparticle VBMs above the other pinning energy of -6.0 eV[42]. We thus can conclude that for 2D heterojunctions of our studied 2D MA_2Z_4 with other semiconductors, the DFT calculation is enough to assess the type of band alignment, and the GW method is necessary to obtain the quantitative band offset or other related properties.

In order to avoid the costly GW calculation on the quantitative band offset, the band-gap-center approximation has been proposed to estimate the absolute quasiparticle band edge energy with the assumption that the self-energy correction shifts both VBM and CBM in inverse direction with similar amounts, such as in monolayer TMDCs[8, 43]. We find that this model is also valid for our studied monolayer MA_2Z_4 ($M = \text{Mo}, \text{W}, \text{Ti}$; $A = \text{Si}, \text{Ge}$; $Z = \text{N}, \text{P}, \text{As}$). The band-gap-center approximation gives nearly the same band edge energy as the costly direct GW calculation in Fig. 2. Taking monolayer MoSi₂N₄ as an example, the VBM (CBM) from band-gap-center model is -6.062 (-2.972) eV, in line with the corresponding value of -6.034 (-2.944) eV from direct GW calculation. On the other hand, one must be cautious when applying the band-gap-center approximation to other MA_2Z_4 . For example, for monolayer CrSi₂N₄, the VBM at around -5.4 eV is almost unchanged by the G_0W_0 self-energy, while the CBM is shifted up by 1.113

eV with the quasiparticle correction. The unchanged VBM may be related to the much larger screened exchange and coulomb hole contribution in CrSi₂N₄ compared with those in MoA₂Z₄ and WA₂Z₄. We note that this asymmetric shift in band edge energy also appears in H-TiCl₂ and T-BiClTe, as a result of the orbital character of the band edge wave function[44].

V. ENVIRONMENTAL SCREENING ON QUASIPARTICLE BAND ALIGNMENT

Generally, environmental screening is expected to decrease the electronic band gap of isolated 2D materials, and thus affect the band alignment accordingly[1, 10, 11]. To investigate the effect of environmental screening on the quasiparticle band alignment, we perform the GW calculation on monolayer MoSi₂N₄ with WSi₂N₄ substrate and compare it to the suspended one. Here, we only use the AA-stacked MoSi₂N₄/WSi₂N₄ heterostructure as an effective model to study the environmental screening effect of WSi₂N₄ on MoSi₂N₄, and other stacking modes will be discussed in section VI.

For AA-stacked MoSi₂N₄/WSi₂N₄, the Mo (Si, N) atoms in one layer fully overlap with the W (Si, N) atoms in the WSi₂N₄ layer. The lattice mismatch is nearly zero, and the optimized layer distance between Mo and W atom is 10.492 Å, much larger than that (6.23–6.54 Å) of bilayer TMDCs, such as MoS₂ and WS₂[45, 46]. This suggests that, compared with bilayer TMDCs, the interlayer vdW interaction in MoSi₂N₄/WSi₂N₄ heterostructure is much weaker, which is owing to the two passivated SiN₂ pyramid layers and has been observed in bilayer MoSi₂N₄[47]. Such weak interlayer interaction leads to no band hybridization between two layers in the band edge of MoSi₂N₄/WSi₂N₄ heterostructure, as shown in Fig. 3a. This is totally different from bilayer or bulk TMDC, where the hybridization of chalcogen p -states at the Γ point results in the crossover from direct band gaps in monolayers to indirect band gaps in multilayers[48]. In detail, the VBM and CBM of MoSi₂N₄/WSi₂N₄ heterostructure are contributed by WSi₂N₄ and MoSi₂N₄ layer, respectively, demonstrating the type-II heterostructure, in agreement with the band alignment analysis in section IV. The VBM is dominated

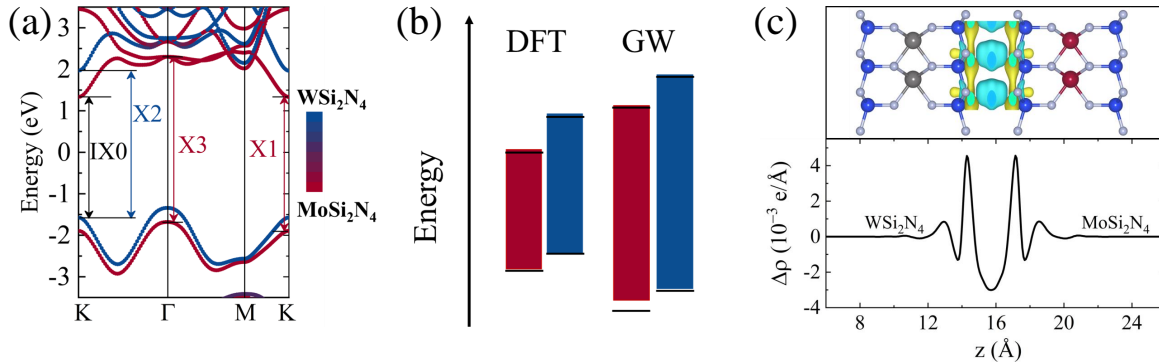


FIG. 3. The quasiparticle band structure of AA-stacked MoSi₂N₄/WSi₂N₄ heterostructure. IX₀, X₁, X₂, and X₃ label the intersubband transitions at K and Γ that give rise to the corresponding excitonic or interband-transition peaks in Fig. 5. (b) Band alignments of monolayer MoSi₂N₄ (WSi₂N₄) in AA-stacked MoSi₂N₄/WSi₂N₄ structure calculated by PBE and GW calculations, where the band alignments of suspended monolayer (black lines) are listed for comparison. The red and blue rectangle represent the band alignments of MoSi₂N₄ and WSi₂N₄, respectively. (c) Plane-averaged charge density difference $\Delta\rho(x)$ of MoSi₂N₄/WSi₂N₄ heterostructure. The top panel is a three-dimensional charge density difference, and the isosurface value is 2×10^{-5} e/ \AA^3 . The yellow and blue areas represent electron accumulation and depletion, respectively.

by W d_{z^2} and $d_{x^2-y^2}$ orbitals, while CBM mainly consists of Mo d_{z^2} orbitals, accompanied by N p orbitals. On the whole, it is clearly shown that the indirect bandgap feature and band dispersion of monolayer MoSi₂N₄ is almost not affected by the WSi₂N₄ substrate, and vice versa. Therefore, the effect of wavefunction overlap may be ignored in MA₂Z₄ monolayers with substrates.

To study the environmental screening effect of WSi₂N₄ (MoSi₂N₄) in MoSi₂N₄/WSi₂N₄ structure, we plot the absolute band edge energies of monolayer MoSi₂N₄ (WSi₂N₄) in MoSi₂N₄/WSi₂N₄ structure in Fig. 3b. The values of VBM and CBM in MoSi₂N₄ are lower than those of WSi₂N₄, demonstrating type-II band alignment of MoSi₂N₄/WSi₂N₄ heterostructure, which is consistent with the projected band structure analysis in Fig. 3a. At the DFT level, the absolute VBM and CBM of monolayer MoSi₂N₄ (WSi₂N₄) in the contact system are very close to those of free-standing sample, with energy difference smaller than 0.05 eV. After including quasiparticle correction, compared with the suspended monolayer, the supported MoSi₂N₄ (WSi₂N₄) possesses almost the same CBM energy, while with higher VBM. The quasiparticle correction pushes up the VBM by 0.153 eV (0.051 eV) for supported MoSi₂N₄ (WSi₂N₄), leading to a 4.9% (1.7%) reduction in quasiparticle band gap compared to free-standing monolayers. Comparing the band edge energies at DFT and GW levels, we can conclude that this environment-induced renormalization of the quasiparticle band gaps is a result of many-body effects on the screening and thus not apparent at the DFT level. On the other hand, the renormalization of the quasiparticle band gap of supported MoSi₂N₄ is the same as the bilayer MoSi₂N₄[49], confirming the reliability of our results. This quasiparticle band gap renormalization is very small in comparison with those of encapsulated monolayer black phosphorus (MoSe₂), whose quasiparticle band gap is reduced by 25% (11%)[1, 10]. The small

renormalization originates from the outer passivated A-Z bilayers in MA₂Z₄, protecting the band edge states from the dielectric screening. In this sense, our absolute band edge energy of isolated monolayer MA₂Z₄ in section IV is still instructive for realistic conditions with surrounded dielectric environment.

Apart from dielectric screening, charge transfer could also affect the band alignment of MoSi₂N₄/WSi₂N₄ heterostructure. In order to quantify this effect, we extract the plane-averaged charge density difference $\Delta\rho(z)$ along the vertical direction (z axis) for MoSi₂N₄/WSi₂N₄ heterostructure in Fig. 3c. Here, $\Delta\rho(z)$ is calculated by the charge density difference between the heterostructure and two noninteracting monolayers. For MoSi₂N₄/WSi₂N₄ heterostructure, the $\Delta\rho(z)$ is on the order of 10^{-3} e/ \AA , which is one order of magnitude smaller than that of typical type-II TMDC heterostructure like PtS₂/MoTe₂[50]. This suggests small charge transfer between layers, consistent with the observed very weak interlayer vdW interaction in MoSi₂N₄/WSi₂N₄ heterostructure. On the whole, we can see clearly that changes in $\Delta\rho(z)$ are almost symmetric on the two sides of the interface. This is very different from the asymmetric $\Delta\rho(z)$ for other bilayers such as strained bilayer MoSi₂N₄ and TMDC[47, 50]. This symmetric charge difference suggests that the charge transfer is very small in MoSi₂N₄/WSi₂N₄ heterostructure, leading to the weak interlayer interaction in MA₂Z₄. It is the negligible charge transfer between the substrate and MA₂Z₄ that results in insignificant substrate effect for MA₂Z₄.

VI. STACKING-INDEPENDENT EXCITONS IN MoSi₂N₄/WSi₂N₄ HETEROSTRUCTURE

In a real MoSi₂N₄/WSi₂N₄ heterostructure, two individual layers have different orientations, forming a twist

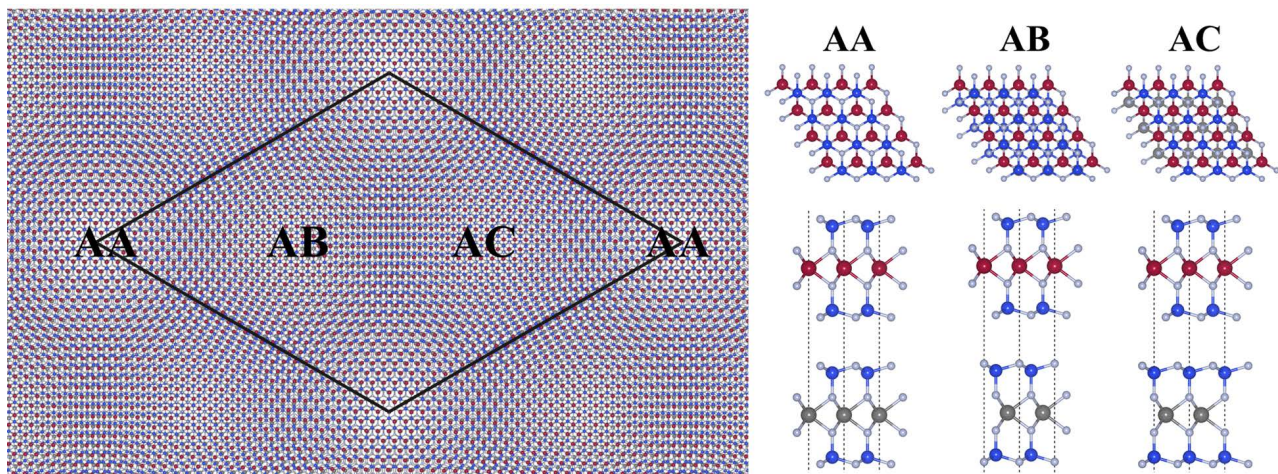


FIG. 4. The schematic plots of $\text{MoSi}_2\text{N}_4/\text{WSi}_2\text{N}_4$ heterostructure rotated from the AA stacking style with a small twist angle (moiré pattern). Three local stacking styles are identified and amplified with top and side views.

angle and a moiré superlattice with a relatively large period. A small-angle moiré superlattice can be viewed as regions of high-symmetry stacking separated by domain walls[51], in which the periodic modulation of local potential give rise to an exciton lattice centered on high-symmetry stacking region forms[52, 53]. Hence, we will pay attention to specific stacking styles and calculate their local exciton properties. As shown in Fig. 4, we take the R type as an example to study the twist-angle dependent exciton properties of twisted $\text{MoSi}_2\text{N}_4/\text{WSi}_2\text{N}_4$ heterostructure. The R type represents a small twist angle rotated from the AA stacking style. In the R type of twisted bilayers, three local stacking styles can be identified in Fig. 4, which have been denoted as AA, AB, and AC, respectively. In the AA configuration, two monolayers are aligned, and all atoms of the same type are superimposed. Based on the AA configuration, the AB and AC configurations are obtained by shifting the bottom WSi_2N_4 layer along the long-diagonal of the unit cell by $1/3$ and $2/3$, respectively. The interlayer distances and relative energies of the three heterostructure structures are given in Table II. Among the three configurations, AA possess the largest interlayer distance (10.492 \AA), and thus the weakest interlayer interaction. The largest interlayer distance is attributed to the repulsion arising from the N atoms superimposing in the two layers, leading to the highest relative energy. Meanwhile, AB and AC configurations share similar and lower interlayer distances and lower relative energies.

We first compare the quasiparticle band structure of the three stacking styles. Similar to AA configuration in Fig. 3a, a typical type-II quasiparticle band alignment is obtained in AB and AC modes. We focus on the band gap at K point, because the vertical inter-band transitions and excitons around these points are likely responsible for optical spectra observed in the $\text{MoSi}_2\text{N}_4/\text{WSi}_2\text{N}_4$ moiré heterostructure. Table II summarizes the GW-calculated quasiparticle band gaps at the K point, which vary with

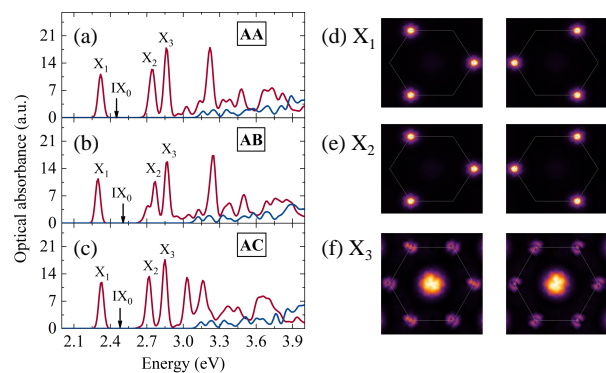


FIG. 5. (a)-(c) Optical absorption spectra of three identified local stacking styles in a $\text{MoSi}_2\text{N}_4/\text{WSi}_2\text{N}_4$ heterostructure with (red) and without e-h (blue) interactions. The energy of the interlayer exciton (IX_0) is marked by the black arrow. A 20-meV smearing to spectral widths is applied. (d)-(f) The reciprocal-space distribution of the charge density of bright exciton X_1 , X_2 , and X_3 .

the local stacking styles. For the R stacking styles, the energy variation is observable: AB mode has the smallest band gap of 2.891 eV , while AC mode possess the largest band gap of 3.057 eV , showing a 166-meV variation of the quasiparticle band gap. This large quasiparticle band gap variation is larger than that (100-meV) of R-type $\text{MoSe}_2/\text{WSe}_2$ twisted bilayers[54].

Figure 5 shows the optical absorption spectra of the three local stacking styles. Like many other 2D structures, enhanced excitonic effects are observed: after including e-h interactions, three excitonic peaks are formed below the quasiparticle band gap with significant e-h binding energies around a few hundred meV. Generally, there are two types of excitons, the intralayer (X_1 , X_2 , and X_3) and interlayer ones (IX_0). To elucidate these features, we break down each exciton state into its com-

TABLE II. Interlayer distance d , relative energy ΔE , band gap, and energy and optical oscillator strength of the excitons for the three different MoSi₂N₄/WSi₂N₄ heterostructures.

	d (Å)	ΔE (meV)	E_g^{DFT} (eV)	E_g^{GW} (eV)	E_{gKK}^{DFT} (eV)	E_{gKK}^{GW} (eV)	X ₁		IX ₀		X ₂		X ₃	
							Energy (eV)	Osc. Str. (a.u.)	Energy (eV)	Osc. Str. (a.u.)	Energy (eV)	Osc. Str. (a.u.)	Energy (eV)	Osc. Str. (a.u.)
AA	10.492	46	1.558	2.771	1.802	2.923	2.327	635	2.451	1.8×10^{-4}	2.757	593	2.864	1672
AB	10.144	0	1.454	2.652	1.706	2.891	2.298	652	2.505	3.1×10^{-4}	2.767	690	2.866	1014
AC	10.144	0	1.643	2.849	1.902	3.057	2.326	662	2.480	0.7×10^{-4}	2.720	562	2.847	1199

ponent transitions. The exciton wave function can be written as a linear combination of electron-hole pairs

$$\Psi_\lambda(r_e, r_h) = \sum_{v\mathbf{c}\mathbf{k}} A_{v\mathbf{c}\mathbf{k}}^\lambda \psi_{\mathbf{c}\mathbf{k}}(r_e) \psi_{v\mathbf{k}}^*(r_h)$$

where $\psi_{\mathbf{c}\mathbf{k}}(r_e)$ ($\psi_{v\mathbf{k}}^*(r_h)$) is the quasi-particle electron (hole) wavefunctions; λ indexes the exciton state; v and c index the occupied and unoccupied bands, respectively; and $A_{v\mathbf{c}\mathbf{k}}^\lambda$ is the electron-hole amplitude.

We now discuss the interlayer exciton (IX₀), marked by the black arrows in Fig. 5. For AA stacking mode, the exciton IX₀ comes primarily from transitions between the VBM and the CBM (Table III), which make up 99% of the band-to-band transitions composing the exciton and confirm the interlayer feature. The interlayer exciton IX₀ is located at 2.451 eV, and the quasiparticle direct band gap is 2.923 eV, resulting in an e-h binding energy of 472 meV. This is similar to the binding energy (410 meV) of MoSe₂/WSe₂ bilayers[54]. On the other hand, the optical oscillator strength of the interlayer exciton is very small (on the order of 10^{-6} times that of the intralayer exciton), as a result of the complete separation of electron and hole wave functions. This dark interlayer exciton is very different from the stacking-dependent interlayer excitons in TMDCs, with dipole oscillator strength reaching the same order as those of intralayer excitons. Moreover, unlike what is normally expected for type-II heterostructures, the interlayer exciton is not the lowest-energy one, owing to the decreased coulomb interaction in the thick MoSi₂N₄/WSi₂N₄ heterostructure. Finally, the energy and brightness of the interlayer exciton are nearly independent of the stacking style in Table II. For example, the interlayer exciton located at 2.451 eV in AA mode, 2.505 in AB mode, and 2.480 eV in AC mode, and the corresponding exciton binding energies are 472, 386, and 577 meV, respectively. The order of the exciton binding energy is consistent with the direct quasiparticle band gap at K point, following the linear scaling law between the exciton binding energies and quasiparticle band gaps observed in 2D materials[7]. This suggests that the moiré superlattice in twisted bilayer MoSi₂N₄/WSi₂N₄ does not modulate the interlayer exciton properties.

There are three main bright exciton peaks X₁, X₂, and X₃ in the optical spectra below the quasiparticle direct gap. The exciton wavefunction shows that the first peak X₁ at lowest-energy (2.327 eV) arises from two degenerate excitonic states, and comes from transitions

TABLE III. Dominant band-to-band transition and its weight $\sum_k |A_{v\mathbf{c}\mathbf{k}}|^2$ of excitons in MoSi₂N₄/WSi₂N₄ heterostructures.

State	Conduction band	Valence band	$\sum_k A_{v\mathbf{c}\mathbf{k}} ^2$
IX ₀	CBM	VBM	0.992
X ₁	CBM	VBM-1	0.989
X ₂	CBM+1	VBM	0.997
X ₃	CBM	VBM-1	0.654

between VBM-1 and CBM (Table III) within MoSi₂N₄ monolayer, indicating the intralayer character. Figure 5 shows the k -resolved e-h pair amplitudes for these two excitonic states, which are dominated by the e-h pairs near the minimum direct gap at K and K' points, similar to that in monolayer MoS₂[4]. While for the second peak X₂ around 2.757 eV, it comes from transitions between VBM and CBM+1, i.e., coming from WSi₂N₄ layer. The exciton X₂ originates from the direct transition at K-point in reciprocal-space exciton wave function. At energies above the second peak, the third peak X₃ is due to the direct transition at Γ point partially coinciding with other direct transition at K point, mainly dominated by MoSi₂N₄ layer. Different from the negligible dipole oscillator strength in dark interlayer exciton, the bright intralayer excitons have large dipole oscillator strength, because of the significant overlap of their electron and hole wave functions. Strikingly, the optical oscillator strengths of these three intralayer excitons (listed in Table II) are robust to the stacking style, having the same order of 10^2 for excitons X₁ and X₂, and the order of 10^3 for exciton X₃. This is very different from the excitons in TDMC moiré supercells, with the optical dipole oscillator strength modulated by a few orders of magnitude. These results are valuable for designing material platforms of Moiré excitons and exciton condensation.

VII. CONCLUSION

In conclusion, we systematically study the quasiparticle band alignment and exciton in monolayer MA₂Z₄ (M = Mo, W, Ti; A = Si, Ge; Z = N, P, As). Compared with the results from DFT, monolayer MA₂Z₄ possess substantially larger quasiparticle band gaps, and the different absolute quasiparticle band alignments accordingly. On the other hand, the band-gap-center model works very well for obtaining the absolute band

edge energy of monolayer MA_2Z_4 , and the qualitative types of band alignments for these materials have not changed from DFT and GW. Based on the obtained band alignments, we design type-II heterostructure $\text{MoSi}_2\text{N}_4/\text{WSi}_2\text{N}_4$ without lattice mismatch and use this mode to discuss the effect of environmental screening and moiré pattern on quasiparticle band alignment and excitons. It is found that the absolute quasiparticle band alignments are robust to the environmental screening, owing to protecting effect of the capped A-Z sublayers in MA_2Z_4 . Finally, we study interlayer and intralayer excitons in $\text{MoSi}_2\text{N}_4/\text{WSi}_2\text{N}_4$ bilayers. Our calculations reveal that the dipole oscillator strength and energy of intralayer excitons are almost independent of the local stacking configuration, suggesting the negligible effect of moiré pattern modulation. The absolute band edge ener-

gies and band offsets obtained in this work are important for designing heterojunction devices based on monolayer MA_2Z_4 .

ACKNOWLEDGEMENT

This work is supported by the National Natural Science Foundation of China (Grant Nos. 12104421 and 11947218). SG is supported as part of the Institute for Quantum Matter, an Energy Frontier Research Center funded by the U.S. Department of Energy, Office of Science, Basic Energy Sciences under Award No. DE-SC0019331. Numerical calculations presented in this paper have been performed on a supercomputing system in the Supercomputing Center of Wuhan University.

-
- [1] M. M. Ugeda, A. J. Bradley, S.-F. Shi, F. H. da Jornada, Y. Zhang, D. Y. Qiu, W. Ruan, S.-K. Mo, Z. Hussain, Z.-X. Shen, *et al.*, *Nat. Mater.* **13**, 1091 (2014).
- [2] K. F. Mak, C. Lee, J. Hone, J. Shan, and T. F. Heinz, *Phys. Rev. Lett.* **105**, 136805 (2010).
- [3] V. Tran, R. Soklaski, Y. Liang, and L. Yang, *Phys. Rev. B* **89**, 235319 (2014).
- [4] D. Y. Qiu, H. Felipe, and S. G. Louie, *Phys. Rev. Lett.* **111**, 216805 (2013).
- [5] C. D. Spataru, S. Ismail-Beigi, L. X. Benedict, and S. G. Louie, *Phys. Rev. Lett.* **92**, 077402 (2004).
- [6] H.-X. Zhong, S. Gao, J.-J. Shi, and L. Yang, *Phys. Rev. B* **92**, 115438 (2015).
- [7] J.-H. Choi, P. Cui, H. Lan, and Z. Zhang, *Phys. Rev. Lett.* **115**, 066403 (2015).
- [8] Y. Liang, S. Huang, R. Soklaski, and L. Yang, *Appl. Phys. Lett.* **103**, 042106 (2013).
- [9] B. Zheng, C. Ma, D. Li, J. Lan, Z. Zhang, X. Sun, W. Zheng, T. Yang, C. Zhu, G. Ouyang, *et al.*, *J. Am. Chem. Soc.* **140**, 11193 (2018).
- [10] D. Y. Qiu, F. H. da Jornada, and S. G. Louie, *Nano Lett.* **17**, 4706 (2017).
- [11] A. J. Bradley, M. M. Ugeda, F. H. da Jornada, D. Y. Qiu, W. Ruan, Y. Zhang, S. Wickenburg, A. Riss, J. Lu, S.-K. Mo, *et al.*, *Nano Lett.* **15**, 2594 (2015).
- [12] L. Li, J. Kim, C. Jin, G. J. Ye, D. Y. Qiu, F. H. da Jornada, Z. Shi, L. Chen, Z. Zhang, F. Yang, *et al.*, *Nat. Nanotechnol.* **12**, 21 (2017).
- [13] G. Zhang, S. Huang, A. Chaves, C. Song, V. O. Özçelik, T. Low, and H. Yan, *Nat. Commun.* **8**, 1 (2017).
- [14] S. Zhang, J. Yang, R. Xu, F. Wang, W. Li, M. Ghufuran, Y.-W. Zhang, Z. Yu, G. Zhang, Q. Qin, *et al.*, *ACS Nano* **8**, 9590 (2014).
- [15] K. Novoselov, o. A. Mishchenko, o. A. Carvalho, and A. Castro Neto, *Science* **353**, aac9439 (2016).
- [16] J. Kunstmann, F. Mooshammer, P. Nagler, A. Chaves, F. Stein, N. Paradiso, G. Plechinger, C. Strunk, C. Schüller, G. Seifert, *et al.*, *Nat. Phys.* **14**, 801 (2018).
- [17] A. K. Geim and I. V. Grigorieva, *Nature* **499**, 419 (2013).
- [18] K. Tran, G. Moody, F. Wu, X. Lu, J. Choi, K. Kim, A. Rai, D. A. Sanchez, J. Quan, A. Singh, *et al.*, *Nature* **567**, 71 (2019).
- [19] E. M. Alexeev, D. A. Ruiz-Tijerina, M. Danovich, M. J. Hamer, D. J. Terry, P. K. Nayak, S. Ahn, S. Pak, J. Lee, J. I. Sohn, *et al.*, *Nature* **567**, 81 (2019).
- [20] J. Choi, M. Florian, A. Steinhoff, D. Erben, K. Tran, D. S. Kim, L. Sun, J. Quan, R. Claassen, S. Majumder, *et al.*, *Phys. Rev. Lett.* **126**, 047401 (2021).
- [21] Y.-L. Hong, Z. Liu, L. Wang, T. Zhou, W. Ma, C. Xu, S. Feng, L. Chen, M.-L. Chen, D.-M. Sun, *et al.*, *Science* **369**, 670 (2020).
- [22] L. Wang, Y. Shi, M. Liu, A. Zhang, Y.-L. Hong, R. Li, Q. Gao, M. Chen, W. Ren, H.-M. Cheng, *et al.*, *Nat. Commun.* **12**, 1 (2021).
- [23] C. Yang, Z. Song, X. Sun, and J. Lu, *Phys. Rev. B* **103**, 035308 (2021).
- [24] S. Li, W. Wu, X. Feng, S. Guan, W. Feng, Y. Yao, and S. A. Yang, *Phys. Rev. B* **102**, 235435 (2020).
- [25] Q. Cui, Y. Zhu, J. Liang, P. Cui, and H. Yang, *Phys. Rev. B* **103**, 085421 (2021).
- [26] B. Mortazavi, B. Javvaji, F. Shojaei, T. Rabczuk, A. V. Shapeev, and X. Zhuang, *Nano Energy* **82**, 105716 (2021).
- [27] J. Yu, J. Zhou, X. Wan, and Q. Li, *New J. Phys.* **23**, 033005 (2021).
- [28] J. P. Perdew, K. Burke, and M. Ernzerhof, *Phys. Rev. Lett.* **77**, 3865 (1996).
- [29] P. Giannozzi, S. Baroni, N. Bonini, M. Calandra, R. Car, C. Cavazzoni, D. Ceresoli, G. L. Chiarotti, M. Cococcioni, I. Dabo, *et al.*, *J. Phys. Condens. Matter* **21**, 395502 (2009).
- [30] A. Otero-De-La-Roza and E. R. Johnson, *J. Chem. Phys.* **136**, 174109 (2012).
- [31] N. Troullier and J. L. Martins, *Phys. Rev. B* **43**, 1993 (1991).
- [32] Z. Wang, X. Kuang, G. Yu, P. Zhao, H. Zhong, and S. Yuan, *Phys. Rev. B* **104**, 155110 (2021).
- [33] M. S. Hybertsen and S. G. Louie, *Phys. Rev. B* **34**, 5390 (1986).
- [34] M. Rohlfing and S. G. Louie, *Phys. Rev. B* **62**, 4927 (2000).
- [35] J. Deslippe, G. Samsonidze, D. A. Strubbe, M. Jain, M. L. Cohen, and S. G. Louie, *Commun. Phys.* **183**, 1269 (2012).

- [36] S. Ismail-Beigi, Phys. Rev. B **73**, 233103 (2006).
- [37] C. A. Rozzi, D. Varsano, A. Marini, E. K. Gross, and A. Rubio, Phys. Rev. B **73**, 205119 (2006).
- [38] C. D. Spataru, S. Ismail-Beigi, L. X. Benedict, and S. G. Louie, Appl. Phys. A: Mater. Sci. Process. **78**, 1129 (2004).
- [39] L. Yang, C. D. Spataru, S. G. Louie, and M.-Y. Chou, Phys. Rev. B **75**, 201304 (2007).
- [40] D. Liang, S. Xu, P. Lu, and Y. Cai, Phys. Rev. B **105**, 195302 (2022).
- [41] H. Ullah, A. A. Tahir, S. Bibi, T. K. Mallick, and S. Z. Karazhanov, Appl. Catal. B **229**, 24 (2018).
- [42] S. Hu, B. Xia, Y.-P. Lin, T. Katase, J. Fujioka, T. Kamiya, H. Hosono, K.-Z. Du, and Z. Xiao, Adv. Funct. Mater. **30**, 1909906 (2020).
- [43] H. Zhong, R. Quhe, Y. Wang, Z. Ni, M. Ye, Z. Song, Y. Pan, J. Yang, L. Yang, M. Lei, *et al.*, Sci. Rep. **6**, 1 (2016).
- [44] A. C. Riis-Jensen, T. Deilmann, T. Olsen, and K. S. Thygesen, ACS Nano **13**, 13354 (2019).
- [45] S. Gao, L. Yang, and C. D. Spataru, Nano Lett. **17**, 7809 (2017).
- [46] J. He, K. Hummer, and C. Franchini, Phys. Rev. B **89**, 075409 (2014).
- [47] H. Zhong, W. Xiong, P. Lv, J. Yu, and S. Yuan, Phys. Rev. B **103**, 085124 (2021).
- [48] Y. Zhang, T.-R. Chang, B. Zhou, Y.-T. Cui, H. Yan, Z. Liu, F. Schmitt, J. Lee, R. Moore, Y. Chen, *et al.*, Nat. Nanotechnol. **9**, 111 (2014).
- [49] Y. Wu, Z. Tang, W. Xia, W. Gao, F. Jia, Y. Zhang, W. Zhu, W. Zhang, and P. Zhang, NPJ Comput. Mater. **8**, 1 (2022).
- [50] S. Yin, Q. Luo, D. Wei, G. Guo, X. Sun, Y. Tang, and X. Dai, Results Phys. **33**, 105172 (2022).
- [51] H. Ochoa, Phys. Rev. B **100**, 155426 (2019).
- [52] D. M. Kennes, M. Claassen, L. Xian, A. Georges, A. J. Millis, J. Hone, C. R. Dean, D. Basov, A. N. Pasupathy, and A. Rubio, Nat. Phys. **17**, 155 (2021).
- [53] H. Yu, G.-B. Liu, J. Tang, X. Xu, and W. Yao, Sci. Adv. **3**, e1701696 (2017).
- [54] X. Lu, X. Li, and L. Yang, Phys. Rev. B **100**, 155416 (2019).